Journal of Fluids and Structures (2000) **14,** 1215–1234
doi:10.1006/jfls.2000.0320, available online at http://www.idealibrary.com on IDEAL®

REDUCED-ORDER MODELS OF UNSTEADY TRANSONIC VISCOUS FLOWS IN TURBOMACHINERY

B. I. Epureanu

Department of Mechanical Engineering, McGill University
Montreal, QC, Canada H3A 2K6

E. H. Dowell and K. C. Hall

Department of Mechanical Engineering & Materials Science, Duke University
Durham, NC 27708, U.S.A.

(Received 12 July 1999, and in final form 27 June 2000)

The proper orthogonal decomposition (POD) technique is applied in the frequency domain to obtain a reduced-order model of the unsteady flow in a transonic turbomachinery cascade of oscillating blades. The flow is described by a inviscid—viscous model, i.e. a full potential equation outer flow model and an integral equation boundary layer model. The nonlinear transonic steady flow is computed first and then the unsteady flow is determined by a small perturbation linearization about the nonlinear steady solution. Solutions are determined for a full range of frequencies and validated. The full model results and the POD method are used to construct a reduced-order model in the frequency domain. A cascade of airfoils forming the Tenth Standard Configuration is investigated to show that the reduced-order model with only 15–75 degrees of freedom accurately predicts the unsteady response of the full system with approximately 15 000 degrees of freedom.

1. INTRODUCTION

Modeling and controlling aeroelastic systems are issues which have held the interest of researchers since the early days of aerospace engineering. In this paper, we investigate unsteady viscous flows in turbomachinery. We focus our attention on modeling of linearized unsteady flows through a cascade of vibrating airfoils. Current computational fluid dynamics (CFD) codes compute time histories and frequency responses for such flows using models with up to 10^4–10^6 degrees of freedom. However, the required computational time of such codes is very long. Thus, these codes are not routinely used for design applications. An alternative way of addressing this problem is to use reduced-order modeling.

A reduced-order model has by definition a smaller number of degrees of freedom than the original CFD model and is typically several orders of magnitude smaller. Ideally, the reduced-order modeling provides accuracy comparable to the original CFD model, but at much less computational cost when used in an aeroelastic analysis. The tradeoff between accuracy and complexity of the model is dependent on the particular application, of course. Nevertheless, using reduced-order modeling in preliminary design and optimization analyses is very promising especially when active control of an aeroelastic system is concerned because most current control strategies require relatively small system models, with 100 degrees of freedom or less.

Although the field of reduced-order modeling is a relatively recent development, there are several distinct techniques that have been developed. Some of these techniques that have

0889–9746/00/111215 + 20 $35.00/0

been used in aeroelasticity and unsteady aerodynamics were mostly based on physical intuition (Greitzer 1976; Moore & Greitzer 1986; Whitehead 1959). These techniques are useful, but they are limited to a small range of parameter variations in the modeled system, such as the reduced frequencies and static and dynamic loads. For example, the actuator disk theory introduced by Greitzer (1976) used the assumption that the spacing between blades in turbomachinery cascades is much smaller than the wavelength of the perturbations flowing through the blade row. These techniques were followed by more recent analyses that use mathematically derived reduced-order models, such as Padé approximants developed from curve fitting the unsteady aerodynamic transfer functions (Dowell 1980; Peterson & Crawley 1988; Ueda & Dowell 1984). Eigenmode summation techniques in the time or frequency domains (Dowell 1995; Hall 1994), and proper orthogonal decomposition (Dowell *et al.* 1999; Epureanu *et al.* 2001; Hall *et al.* 1999; Romanowski 1996) are the most recent and powerful of such methods.

Most of the recent research on reduced-order modeling has focused on dynamically linearized systems. However, the techniques developed have been used to model both linear and nonlinear phenomena (Noor 1994; Stone & Cutler 1996). The dynamically linearized reduced-order modeling technique has been applied to a wide variety of systems, such as Burger's model of turbulence (Canuto *et al.* 1988; Chambers *et al.* 1988), full potential equation (Hall *et al.* 1995), Euler equations, Navier–Stokes equations (Deane *et al.* 1988), Raleigh–Bénard convection (Holmes *et al.* 1996), turbulence, and boundary layer models (Liu *et al.* 1994; Sirovich 1987a, b, c). Additionally, fully nonlinear normal modes and reduced-order models were also investigated for low-dimensional systems (Shaw & Pierre 1993, 1994).

In the time domain, reduced-order models have been developed for a variety of systems. Flows over isolated airfoils described by the Navier–Stokes equations have been investigated by Romanowski (1996). In his analysis, the Navier–Stokes equations were used in conjunction with eigenmode summation techniques (Mahajan *et al.* 1991) to construct reduced-order models. Recently, the frequency domain has been more extensively analyzed in experiments, full computer fluid dynamics calculations, and reduced-order model construction (Ayer & Verdon 1998; Buffum *et al.* 1998; Kim *et al.* 1997; Kim 1998; Sharma *et al.* 1992). Experiments using a cascade of blades vibrating sinusoidally with small amplitudes have been performed. Also, dynamically linearized frequency domain models have been constructed along with frequency domain reduced-order models. The inviscid full-potential equation in the frequency domain was also used to construct reduced-order models for flows in turbomachinery cascades (Hall *et al.* 1995). Most of the work on reduced-order modeling has been focused on inviscid, subsonic flows. However, recent studies have investigated inviscid transonic flows over isolated airfoils and rows of flat plates in turbomachinery (Hall *et al.* 1999). A coupled inviscid–viscous model using the full-potential equation and a finite difference boundary layer model was also used together with an eigenmode summation technique to construct reduced-order models of the flow in a compressor cascade (Florea *et al.* 1998).

One of the techniques used to construct reduced-order models is proper orthogonal decomposition (POD), also known as the Karhunen–Loève method. This is a technique that allows one to obtain good approximations of the spatial modes of vibration and the dynamics of a system using the response of the system to various sample excitations. First introduced in the context of meteorology and wind engineering to analyze experimental data (Cenedese *et al.* 1997; Jeong & Bienkiewicz 1997; Kikuchi *et al.* 1997; Sahan *et al.* 1997; Tamura *et al.* 1997), proper orthogonal decomposition has been used for a wide variety of problems (Bienkiewicz 1996; Ho *et al.* 1995; Uematsu *et al.* 1997). The wide applicability of the method is due to the fact that it is only based on the assumption of a low dimensionality

of the dynamics of large systems (Chambers *et al.* 1988; Georgiou & Schwartz 1996). For a large category of problems, this assumption holds because in many cases the energy of the dynamics of the system being analyzed is, to a very large extent, contained in the dynamics of a few modes of vibration. In the context of aeroelasticity, if one only wants the aerodynamic information *per se*, then constructing the POD model takes about as much time as the original method. However, if one wants to combine the aerodynamic model with a structural model (not to mention an active control system), then the time saved is orders of magnitude larger, because one is using a POD model with less than 100 degrees of freedom (as shown in this paper) versus using the original CFD model with more than 10 000 degrees of freedom. Thus, it is in the aeroelastic analysis that the time savings are primarily realized, not in generating the aerodynamic data *per se*. The purpose of constructing a POD model is then to put the basic physics of the original CFD model in a more compact form that is advantageous to those who do aeroelastic analyses.

In the context of turbulent flows, proper orthogonal decomposition was adopted as a technique that allows for the identification of coherent structures that naturally form in the flow (Holmes *et al.* 1996; Sirovich 1987a, b, c). The coherent structures that contain most of the energy of the dynamics are usually the most important. Very well suited for linear systems, proper orthogonal decomposition is also applicable to nonlinear systems. However, for some nonlinear systems, the applicability of proper orthogonal decomposition method is limited because the modes or coherent structures strongly exchange energy and, therefore, the required number of modes that may capture most of the energy of the dynamics increases very rapidly. This phenomenon occurs because the inherent dynamics of the system is not low dimensional (Strain & Greenside 1998). Typical examples where the simple proper orthogonal decomposition technique is not successful are systems that exhibit spatio-temporal chaos. However, in such situations, proper orthogonal decomposition may also be used in a local fashion. When spatio-temporal chaos is present, usually there are unstable limit cycles embedded in the strange attractor on which the dynamics collapses. The dynamics along these limit cycles is low dimensional and therefore local reduced-order models may be constructed. Using the low-dimensional approximate dynamics along the limit cycles one may design controllers that will stabilize these limit cycles (Epureanu & Dowell 1997, 1998; Epureanu *et al.* 1998).

In this paper, a fully nonlinear steady model and an unsteady model developed from dynamic linearization of the inviscid–viscous transonic flow in a turbomachinery cascade is developed. The inviscid transonic outer flow is described by the full-potential equation using a Galerkin formulation (Hall 1993). The viscous flow in the boundary layer is described by an integral boundary layer model (Cizmas 1995; Cizmas & Hall 1995; Drela 1986; Nishida & Drela 1995) based on a set of correlation functions derived by Drela (1986) from analytical, numerical and experimental data. First, the nonlinear steady flow is computed. Then, the unsteady flow equations are dynamically linearized about the nonlinear steady flow solution. A frequency domain, dynamically linearized model is constructed, and the proper orthogonal decomposition technique is applied in the frequency domain to obtain a reduced-order model. While the simultaneous inviscid–viscous coupling solution method is a well-established approach, the use of the proper orthogonal decomposition (POD) method for such inviscid/viscous models is new and a novel contribution of this paper. Numerical results obtained with the present full model are compared with those from Navier–Stokes calculations to validate the underlying physical basis for the present model. A reduced-order model obtained using only 15–75 degrees of freedom is then shown to capture accurately the dynamics of the transonic, viscous, small-disturbance flow of the present full model.

2. MODELING

First introduced by Prandtl, the boundary layer assumption is used here. In many cases of interest, the Reynolds number is very large and the effect of the viscosity is limited to a thin region around the solid boundaries and the wake, also known as a boundary or inner layer. The flow is decomposed into an inviscid outer flow and a viscous inner flow. In the following, we present the inviscid model, the viscous model, and the coupling solution technique used.

2.1. Inviscid Outer Flow

For a homentropic and irrotational flow, the velocity vector is the gradient of a scalar potential function. For the case of inviscid and nonheat-conducting flow, the potential satisfies the full-potential equation, which may be expressed as

$$\nabla^2\phi = \frac{1}{c^2}\left[\frac{\partial^2\phi}{\partial t^2} + 2\nabla\phi\cdot\nabla\,\frac{\partial\phi}{\partial t} + \frac{1}{2}\,\nabla\phi\cdot\nabla(\nabla\phi)^2\right], \tag{1}$$

where c is the local speed of sound given by

$$c^2 = c_0^2 - (\gamma-1)\left[\frac{\partial\phi}{\partial t} + \frac{1}{2}\,(\nabla\phi)^2\right] \tag{2}$$

with c_0 denoting the stagnation speed of sound and γ the ratio of specific heats. Equation (1) may also be written in conservative form as

$$\frac{\partial\rho}{\partial t} + \nabla\cdot(\rho\nabla\phi) = 0, \tag{3}$$

where ρ is the density, which is expressed in terms of the potential as

$$\rho = \rho_T\left\{1 - \frac{(\gamma-1)}{c_0^2}\left[\frac{\partial\phi}{\partial t} + \frac{1}{2}\,(\nabla\phi)^2\right]\right\}^{1/(\gamma-1)}. \tag{4}$$

In this work, we discretize the potential using a finite element method. We used a computational grid comprised of isoparametric quadrilateral bilinear elements. The value of the potential ϕ inside a finite element is related to the value of the potential ϕ_i at the four corners of the element by a bilinear isoparametric interpolation given by

$$\phi(\xi,\eta,t) = \sum_{i=1}^{4} N_i(\xi,\eta)\,\phi_i(t), \tag{5}$$

where N_i are four interpolation functions, and ξ and η are the local coordinates inside the finite element. In the Galerkin weighted-residual method, an integral formulation is used in the form

$$\int\!\!\int_D \left[\frac{\partial\rho}{\partial t} + \nabla\cdot(\rho\nabla\phi)\right] N_i\,\mathrm{d}x\,\mathrm{d}y + \oint\left(Q - \rho\,\frac{\partial\phi}{\partial\mathbf{n}}\right) N_i\,\mathrm{d}\xi = 0, \tag{6}$$

where Q is the prescribed mass flux on the boundary and ξ is the distance along the boundary, and $\mathbf{n}$ is the local normal direction at the boundary of the domain over which the full-potential equation is solved.

The Galerkin formulation in equation (6) was used to solve both the steady and the unsteady problems. The small disturbance assumption was used to solve the dynamically

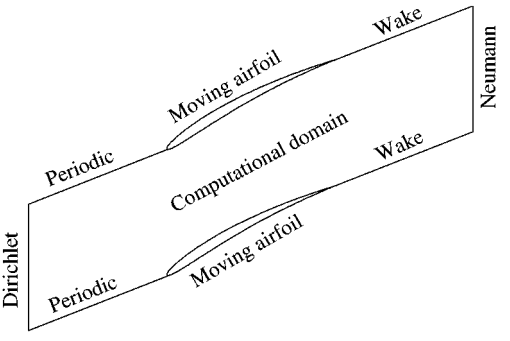

Figure 1. Solution domain used to calculate the inviscid flow in one stage of a cascade. There are five types of boundary conditions that apply to the flow: moving airfoil, periodic, wake, upstream far field and downstream far field.

linearized unsteady problem. The potential was decomposed into a steady value Φ and an unsteady small disturbance potential φ periodically varying in time, such that

$$\phi(x, y, z, t) = \Phi(x, y, z) + \Re[\varphi(x, y, z)\, e^{j\omega t}], \tag{7}$$

where $\varphi \ll \Phi$, $j = \sqrt{-1}$ is the imaginary unit, and $\Re$ denotes the real part.

Figure 1 shows the domain where the flow is solved and the regions where different boundary conditions apply. On the airfoil boundary, we require that the flux Q be equal to

$$Q = Q_{\text{airfoil}} = \rho \frac{\partial \phi}{\partial \mathbf{n}}, \tag{8}$$

which arises from the motion of the airfoil and the thickening of the viscous boundary layer, and $\mathbf{n}$ is the local normal direction to the airfoil surface. The periodicity on the upstream region reads

$$\phi_{\text{up}} = \phi_{\text{down}}\, e^{j\sigma}, \tag{9}$$

where σ is the interblade phase angle. The wake boundary condition states that the jump in pressure across the wake is zero, so that

$$p_{\text{up}} - p_{\text{down}} = 0. \tag{10}$$

Because the computation domain is not perfectly aligned with the wake, an additional injection flux is applied on the wake boundaries

$$Q_{\text{wake}} = \rho u \frac{\partial r}{\partial \xi} + \rho \frac{\partial r}{\partial t}, \tag{11}$$

where u is the tangential velocity along the wake and r is the displacement of the wake with respect to the boundary of the computational domain. For the steady problem, the upstream and downstream boundary conditions are Dirichlet and Newman, respectively. For the unsteady problem, they are exact nonreflecting boundary conditions (Hall *et al.* 1993) for the linearized unsteady problem.

2.2. Viscous Boundary Layer Flow

The boundary layer equations may be obtained performing a scale analysis under the assumption of a very large Reynolds number. In such an analysis, the diffusion process

parallel to a body surface and wake may be neglected and the momentum equation normal to the surface may be replaced by the condition of zero normal pressure gradient throughout the boundary layer. In this analysis, the local airfoil and wake curvature effects are neglected along with the local deformation of the airfoil. Only the rigid-body motion of the airfoil is analyzed.

The two unsteady compressible equations that describe the flow in the thin boundary layer are

$$\frac{\partial \rho}{\partial t} + \frac{\partial (\rho u)}{\partial \xi} + \frac{\partial (\rho v)}{\partial \eta} = 0, \tag{12}$$

$$\frac{\partial (\rho u)}{\partial t} + \frac{\partial (\rho u^2)}{\partial \xi} + \frac{\partial (\rho uv)}{\partial \eta} + \frac{\partial p}{\partial \xi} - \frac{\partial \tau}{\partial \eta} = 0, \tag{13}$$

where ξ and η are now the tangential and normal directions to the surface of the body (Figure 2) while u and v are the tangential and normal components of the velocity.

Formally integrating the mass conservation and momentum equations, one obtains the von Kármán momentum integral equation given by

$$\frac{\partial}{\partial t}\left[\rho_e u_e(\delta^* - \delta_\rho)\right] + \frac{\partial}{\partial \xi}\left(\rho_e u_e^2 \theta\right) + \rho_e \delta_\rho \frac{\partial u_e}{\partial t} + \rho_e u_e \delta^* \frac{\partial u_e}{\partial \xi} - \frac{\rho_e u_e^2}{2} C_f + u_e Q_{\mathrm{bl}} = 0. \tag{14}$$

Similarly, the integral energy equation is

$$\frac{\partial}{\partial t}\left[\rho_e u_e^2(\theta + \delta^* - \delta_\rho)\right] + \frac{\partial}{\partial \xi}\left(\rho_e u_e^3 \theta^*\right) + 2\rho_e u_e(\delta_\rho - \delta)\frac{\partial u_e}{\partial t} + 2\rho_e u_e^2 \delta^{**}\frac{\partial u_e}{\partial \xi} - 2\rho_e u_e^3 C_D + u_e^2 Q_{\mathrm{bl}} = 0, \tag{15}$$

where C_f is the wall shear stress coefficient, Q_{bl} is the wall transpiration due to the boundary layer displacement thickness, and the subscript e indicates quantities measured at the boundary between the inviscid and viscous regions.

The formal integration leads to a number of unknown quantities such as the density thickness δ_ρ, the coefficient of dissipation C_D, the kinematic density displacement δ^{**}, etc. These quantities are described in terms of only two variables, θ and δ^*, by assuming prescribed shapes for the velocity profile inside the boundary layer. Based on both analytical solutions of simple flows and experimental data, many researchers have developed correlation functions (Drela 1986; Nishida & Drela 1995; LeBalleur 1978; Veldman 1979; Whitfield *et al.* 1981) that describe the relationship between θ and δ^* and all the unknown quantities from equations (14) and (15). The correlations used include semi-empirical and empirical relationships between various integral boundary layer characteristics, including

$$\delta = \int_0^\infty \left(1 - \frac{u}{u_e}\right) \mathrm{d}\eta, \qquad \theta = \int_0^\infty \left(1 - \frac{u}{u_e}\right) \frac{\rho u}{\rho_e u_e} \mathrm{d}\eta,$$

$$\delta^* = \int_0^\infty \left(1 - \frac{\rho u}{\rho_e u_e}\right) \mathrm{d}\eta, \qquad \theta^* = \int_0^\infty \left[1 - \left(\frac{u}{u_e}\right)^2\right] \frac{\rho u}{\rho_e u_e} \mathrm{d}\eta,$$

$$\delta^{**} = \int_0^\infty \left(1 - \frac{\rho}{\rho_e}\right) \frac{u}{u_e} \mathrm{d}\eta, \qquad \delta_\rho = \int_0^\infty \left(1 - \frac{\rho}{\rho_e}\right) \mathrm{d}\eta,$$

$$C_D = \frac{1}{\rho_e u_e^3} \int_0^\infty \tau_{\mathrm{wall}} \frac{\partial u}{\partial \eta} \mathrm{d}\eta, \qquad C_f = \frac{2}{\rho_e u_e^2} \tau_{\mathrm{wall}},$$

where τ_{wall} is the tangential wall shear stress.

Laminar-turbulent transition is of considerable practical interest because it strongly influences where separation occurs. The Orr–Somerfeld equation which governs the growth and decay of infinitesimal waves in the shear layer was used in combination with the e^n method to determine the transition. The e^n method correlates the position of the transition to the position where the overall maximum amplification of Tollmien–Schlichting disturbances is e^n. We used the approximate spatial amplification curve derived by Drela (1986) based on the Orr–Somerfeld equation applied to a Falkner–Skan profile family.

The only parameter of the two boundary layer equations (14) and (15) which involves Reynolds stresses is the velocity weighted integral in C_D. Due to the experimental evidence for upstream history effects on the Reynolds stresses, Drela introduced a lag equation that correlates the dissipation factor to the shear stress coefficient given by

$$C_\tau = \frac{1}{u_e^2}\,\overline{u'v'}_{\max}, \tag{16}$$

where $\overline{u'v'}_{\max}$ is the maximum Reynolds stress. The lag equation for the Reynolds shear stress scale was developed by Green (Green 1976; Green *et al.* 1976), starting from Bradshaw's simplified model of the turbulence kinetic energy transport equation. Following the work of Drela (1986), we used this equation together with correlations for the equilibrium, self-preserving flow shear stress and edge velocity gradient

$$\frac{\delta}{u_e^3 C_\tau U_{\max}}\frac{\partial}{\partial t}(u_e^2 C_\tau) + \frac{\delta}{u_e^2 C_\tau}\frac{\partial}{\partial \xi}(u_e^2 C_\tau) + K_c(C_\tau^{1/2} - C_{\tau eq}^{1/2}) = 0, \tag{17}$$

where $U_{\max}$ is the equilibrium slip velocity at the location of maximum shear stress, $C_{\tau eq}$ is the equilibrium shear stress coefficient, and $K_c = 5{\cdot}6$ is an empirical constant (Drela 1996).

The solution domain used to compute the viscous flow is shown in Figure 2, where the thickness of the domain is considered small in comparison to the gap. The steady integral boundary layer equations are parabolic in space so that boundary conditions have to be applied only at the stagnation point. Close to the stagnation point, the flow is similar to a flow over a wall. There is an analytical similarity solution for this flow that relates the displacement thickness to the inviscid tangential velocity (Cebeci & Bradshaw 1977). This similarity solution was used as boundary condition at the stagnation point.

The reduced frequencies associated with the unsteadiness in the inner, boundary layer flow are much higher than the reduced frequencies associated with the outer, inviscid flow due to the large difference in length scales, i.e. the difference between the chord and the boundary layer thickness. Thus, we have extended Drela's (1986) correlations on a

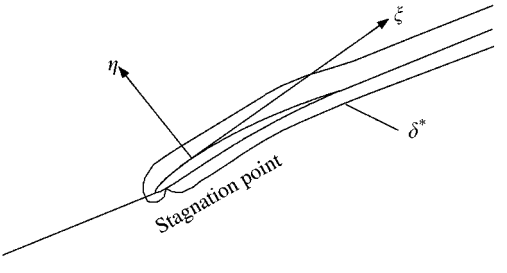

Figure 2. Solution domain used to calculate the viscous flow in one stage of a cascade. A special local analytical solution is used at the stagnation point.

quasi-steady basis by assuming that the unsteadiness in the boundary layer is quasi-steady. The dynamic linearization of the inner, boundary layer equations was performed by linearizing Drela's correlations with respect to the primary boundary layer variables, i.e. δ^*, θ and C_τ.

2.3. Viscous–Inviscid Coupling

Some of the early coupling solution techniques proposed in the literature solved separately the viscous and inviscid regions in an alternate iterative fashion. This technique is known as the direct coupling method and is most useful for weakly interacting flows, e.g. flows with thin boundary layers. The direct coupling method works well, but it converges slowly or fails to converge for strongly interacting flows. Various techniques have been developed to improve and accelerate the convergence of inviscid–viscous interaction methods. These techniques may be classified as inverse (Catherall & Mangler 1966). semi-inverse (LeBalleur 1978), quasi-simultaneous (Veldman 1979, 1981) and simultaneous. In this paper, we used a fully simultaneous technique which solves both the viscous and inviscid regions simultaneously using the tangential velocity at the displacement body and the transpiration velocity to account for the displacement thickness. As opposed to the other techniques, no iterations are required in the fully simultaneous method once the simultaneous set of equations is solved.

The coupling between the inviscid and viscous regions is of major importance, especially at the trailing edge where the Kutta condition applies. The tangential inviscid velocity has a strong variation in this region, therefore having not only a local effect, but also a global effect on the characteristics of the flow. The inviscid–viscous coupling was implemented using an injection velocity also known as wall transpiration. This velocity is equal and of opposite sign to the entrainment velocity, and may be obtained starting from the continuity equation in defect form

$$\frac{\partial(\rho_{\text{inv}} - \rho)}{\partial t} + \frac{\partial(\rho_{\text{inv}} u_{\text{inv}} - \rho u)}{\partial \xi} + \frac{\partial(\rho_{\text{inv}} v_{\text{inv}} - \rho v)}{\partial \eta} = 0, \tag{18}$$

where the subscript inv indicates inviscid variables. Under the assumption of a first-order match at the boundary layer, one concludes that $\rho_e = \rho_{\text{inv}}$ and $u_e = u_{\text{inv}}$. Also, the component of the velocity normal to the surface is expanded in a Taylor series and only the first two terms are retained. Finally, imposing the matching condition at the body surface, one obtains

$$Q_{\text{bl}} = \frac{\partial(\rho_e \delta_\rho)}{\partial t} + \frac{\partial(\rho_e \delta^* u_e)}{\partial \xi}. \tag{19}$$

On the airfoil, the transpiration flux is added to the injection due to airfoil motion. In the wake, the transpiration flux is added to the injection due to the motion of the wake.

3. UPWINDED TRANSONIC GALERKIN FORMULATION

There have been many studies of the transonic full-potential equation, e.g. one of the early pioneers being Murman (Murman & Cole 1971). The Galerkin technique is well-posed for all domains where the governing full-potential equation is elliptic. In the supersonic region, however, the governing equation is hyperbolic. To account for the change in characteristics of the equation, the artificial compressibility method developed by Hafez (Hafez *et al.* 1979; Tatum 1983) is used. Using this technique, the local density used in computing the elemental

residual for an element e is modified in the supersonic and transonic regions. The new density may be expressed as

$$\tilde{\rho}^e = \rho^e - v(\rho^e - \rho^{e-1}), \tag{20}$$

where $e-1$ is the neighbor element located upwind with respect to element e and v is an upwinding coefficient. Many formulas have been proposed for the coefficient v (Habashi & Hafez 1982; Habashi *et al.* 1985; Hafez *et al.* 1979; Murman & Cole 1971). In this work, we used the relation proposed by Whitehead & Newton (1985) and investigated by Giles (1985) and Cedar & Stow (1985), i.e.

$$\begin{aligned} v &= v_0 + v_1 \left(1 - \frac{1}{M^2}\right) \quad \text{when } M \geq 1, \\ v &= v_0 M^{2v_1/v_0} \exp[-\lambda(M-1)^2] \quad \text{when } M < 1, \end{aligned} \tag{21}$$

where M is the local Mach number, v_0 is typically 0·3, v_1 is approximately 1, and λ is usually 20. The formula for the upwinding coefficient for the supersonic region represents upwinding of the flux $\rho\nabla\phi$, and may be obtained by a Taylor expansion of the flux $\rho\nabla\phi$ as a function of the spatial coordinates along a streamline (Giles 1985; Tannehill *et al.* 1997).

4. CODE VALIDATION

The Tenth Standard Configuration (Fransson & Verdon 1993) is used to validate the results obtained with the inviscid–viscous computer code. This configuration is a generic compressor cascade geometry. The airfoils in the cascade have a circular arc camber line with 5% camber and a modified NACA-0006 thickness distribution. The chord of the airfoils is denoted by c, the gap between the airfoils is denoted by G. A solidity G/c of 1 is considered. The stagger angle γ is 45°. The upstream far-field Mach number M is 0·8, the inflow angle Θ is 55°, and the Reynolds number based on chord and upstream velocity Re is 5×10^5. For this configuration, there is a shock expanding into the steady flow on the pressure side of the airfoils. The shock is located at approximately 25% of the chord and does not extend over

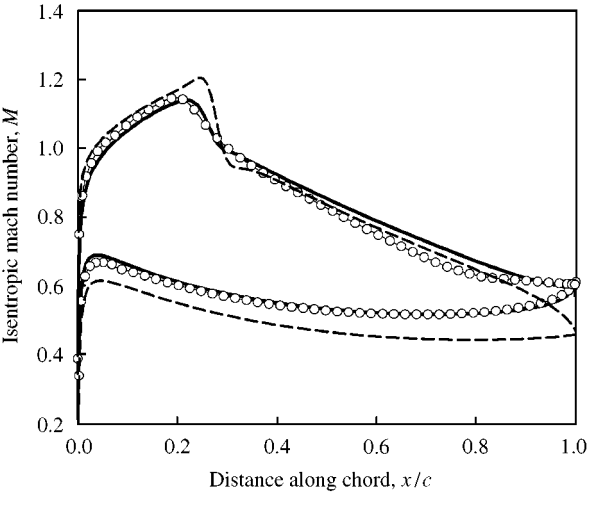

Figure 3. Isentropic Mach number on the airfoil for steady flow and an inlet Mach number of 0·8: —, Navier–Stokes; ○—○, inviscid–viscous; - - -, inviscid.

the entire gap. The isentropic Mach number on the surface of the airfoil is shown in Figure 3. This figure shows that the Mach number obtained using the inviscid–viscous interaction computer code agrees fairly well with the Mach number obtained using a Navier–Stokes code (Clark 1998). Differences in the results are observed close to the trailing edge where the inviscid–viscous calculation predicts a flatter Mach number distribution along the chord. The shock location and strength, however, are shown to agree very well. In contrast, the Mach number predicted by an inviscid calculation, also shown in Figure 3, differs significantly from the viscous calculations confirming that viscous effects are significant in this flow regime.

The dynamically linearized unsteady response of the flow to a periodic pitching oscillation of the cascade of blades about the mid-chord point, with a reduced frequency $k = 0{\cdot}5$ and an interblade phase angle $\sigma = 90^{\circ}$, is shown in Figures 4 and 5. The reduced frequency

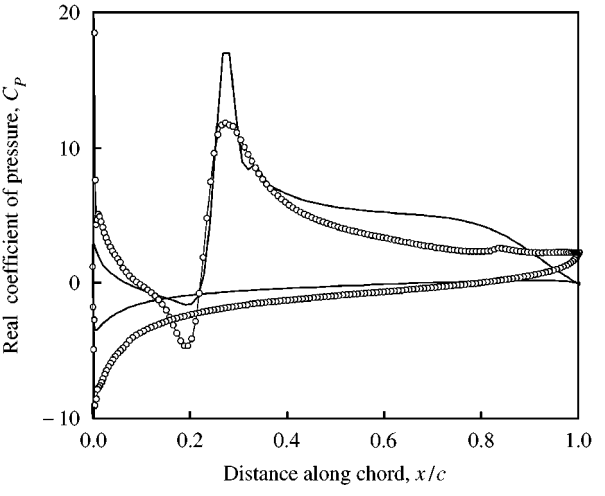

Figure 4. The real (in-phase) part of the unsteady coefficient of pressure C_P for a pitching motion about the mid-chord: —, linearized Navier–Stokes; ○—○, inviscid–viscous.

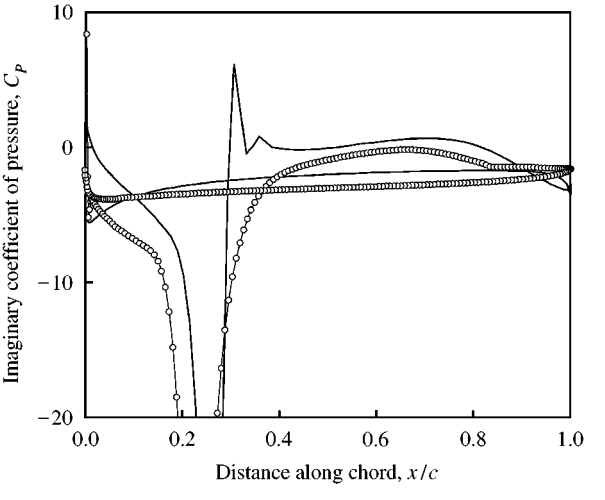

Figure 5. The imaginary (out-of-phase) part of the unsteady coefficient of pressure C_P for a pitching motion about the mid-chord: —, linearized Navier–Stokes; ○—○, inviscid–viscous.

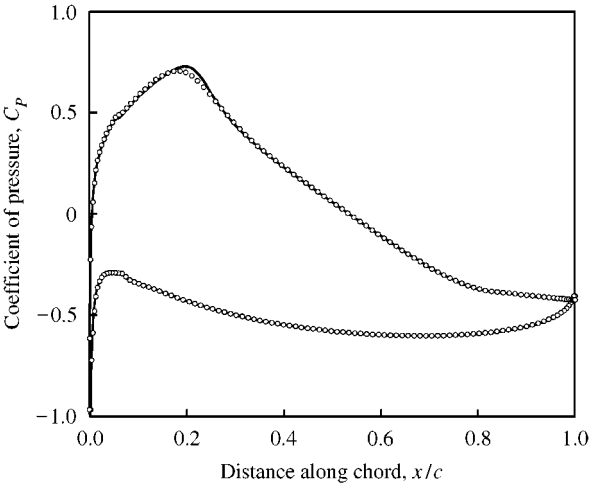

Figure 6. Coefficient of pressure C_P for steady flow using a fine and a coarse grid. —, Fine grid; ○, coarse grid.

k is defined as $k = \omega c/v_\infty$, where c is the chord and v_∞ is the total velocity upstream in the far field. The results obtained using the inviscid–viscous calculation agree reasonably well with the linearized Navier–Stokes results (Clark 1998). While the differences in the steady response were very small, the unsteady flow calculations using the two methods differ more significantly. However, the general trend and magnitude of the results agree reasonably well.

The results presented are not sensitive to grid refinement. Figure 6 shows the steady coefficient of pressure obtained with a coarse and a fine grid. The fine grid has 50×300 nodes, and the coarse grid has 30×200 nodes. Figures 7 and 8 show the in-phase and out-of-phase components of the coefficient of pressure for a pitching motion of the airfoils about their mid-chord with a reduced frequency $k = 0{\cdot}5$ and an interblade phase angle $\sigma = 90^\circ$. The results obtained using the two grids, while not in exact agreement, agree reasonably well. Clearly, grid resolution alone does not account for the differences between the inviscid–viscous and linearized Navier–Stokes calculations.

Finally, another self-consistency test may be performed to check the validity of the linearization. In this test, unsteady results are computed by two different methods. First, results are obtained for the nominal geometry of the cascade using the dynamically linearized perturbation approach with the frequency of perturbation set to zero. In the second approach, results are obtained using the nonlinear steady flow solver for a geometry that is obtained from the nominal geometry by imposing a small rotation about the mid-chord of the airfoils. Dividing the difference between the steady results for the nominal and new geometries by the magnitude of the small rotation about the mid-chord point gives a finite difference approximation of the linearized perturbation response (at zero frequency and zero interblade phase angle). A comparison of the results from these two different methods is presented in Figure 9. The perturbation results are shown to agree very well with those from the finite difference approximation. The error made in approximating the unsteady response by finite differences is of the order of the truncation error, while the error due to the various computations is of the order of the round-off error.

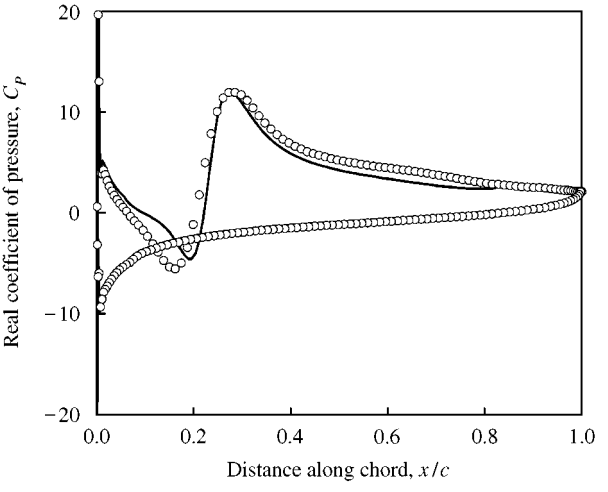

Figure 7. The real (in-phase) part of the unsteady coefficient of pressure C_P for a pitching motion about the mid-chord using a fine and a coarse grid. —, Fine grid; ○, coarse grid.

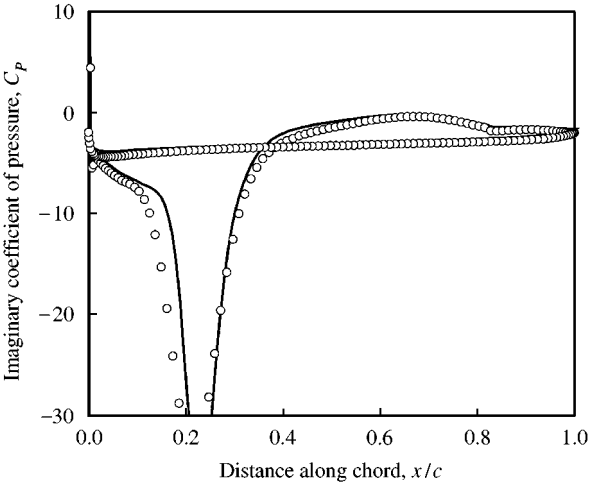

Figure 8. The imaginary (out-of-phase) part of the unsteady coefficient of pressure C_P for a pitching motion about the mid-chord using a fine and a coarse grid. —, Fine grid; ○, coarse grid.

5. PROPER ORTHOGONAL DECOMPOSITION

First introduced in the time domain (Romanowski 1996), proper orthogonal decomposition (POD) has recently been used also in the frequency domain (Epureanu *et al.* 2001; Hall *et al.* 1999; Kim 1998). In this paper, we used the "snapshot" proper orthogonal decomposition method. In this approach, the response of the linearized system with L degrees of freedom is obtained and stored in a solution vector $\boldsymbol{\Phi}_i$, for a set of N excitation frequencies ω_i. Each solution vector $\boldsymbol{\Phi}_i$ has L complex entries and, therefore, contains both the phase and the magnitude of the response. A matrix $\mathbf{R}$ of size $L \times N$ is formed such

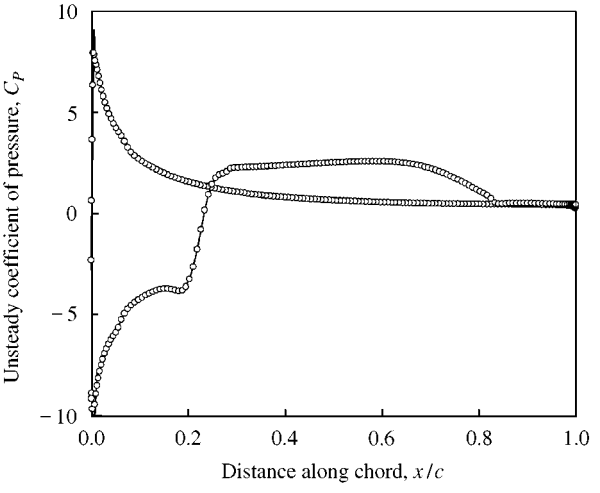

Figure 9. Unsteady coefficient of pressure C_P for a pitching motion about the mid-chord at zero frequency. —, Perturbation analysis; ○—○, finite difference approximation from nonlinear steady flow solver.

that its ith column is the solution vector $\boldsymbol{\Phi}_i$ for each $i \leq N$. A correlation matrix is then assembled in the form

$$\mathbf{C} = \mathbf{R}^*\mathbf{R}, \tag{22}$$

where the superscript $*$ indicates the Hermitian operator. The eigenvalues of the correlation matrix are then obtained by solving an eigenvalue problem of dimension $N \times N$, i.e.

$$\mathbf{C}\mathbf{v}_i = \lambda_i \mathbf{v}_i, \tag{23}$$

where i varies between 1 and N, λ is the reduced-order eigenvalue, and $\mathbf{v}_i$ are eigenvectors of dimension N. Among the POD eigenvalues obtained, the largest eigenmodes contain most of the energy of the fluid motion. The reduced-order modes $\mathbf{v}_i$ and eigenvalues are, therefore, organized in descending order, that is, from the most important to the least important.

The most significant n modes are then grouped in a matrix $\mathbf{V}$ of size $N \times n$ such that the ith column of $\mathbf{V}$ is the vector $\mathbf{v}_i$, $i = 1, \ldots, n$. The equations of motion and the state-space vector are then projected onto the space spanned by these vectors and a reduced-order model is obtained. Formally, one may express the dynamically linearized equations of motion as

$$\omega^2 \mathbf{A}_2 \boldsymbol{\Phi} + \omega \mathbf{A}_1 \boldsymbol{\Phi} + \mathbf{A}_0 \boldsymbol{\Phi} = \mathbf{b}, \tag{24}$$

where $\mathbf{b}$ is the inhomogeneous forcing vector arising from the motion of the airfoil. Multiplying of equation (24) the left-hand side by the Hermitian of the projection matrix $\mathbf{P} = \mathbf{RV}$, and considering only the solutions contained in the subspace $\mathbf{S}$ spanned by the columns of $\mathbf{P}$, one obtains a reduced-order system of size n, i.e.

$$\omega^2 \mathbf{P}^*\mathbf{A}_2\mathbf{P}\tilde{\boldsymbol{\Phi}} + \omega \mathbf{P}^*\mathbf{A}_1\mathbf{P}\tilde{\boldsymbol{\Phi}} + \mathbf{P}^*\mathbf{A}_0\mathbf{P}\tilde{\boldsymbol{\Phi}} = \mathbf{P}^*\mathbf{b}, \tag{25}$$

where $\tilde{\boldsymbol{\Phi}}$ is the component of the solution $\boldsymbol{\Phi}$ in the subspace $\mathbf{S}$, so that

$$\boldsymbol{\Phi} = \mathbf{P}\tilde{\boldsymbol{\Phi}}. \tag{26}$$

Equation (25) represents the reduced-order model, which is solved for the n unknowns $\tilde{\boldsymbol{\Phi}}$. These unknowns are then expanded back into the original physical space using equation

(26). One important feature of the proper orthogonal decomposition technique is that the eigenvalues of the reduced-order model in equation (25) are good approximations of the eigenvalue of the full system.

6. REDUCED-ORDER MODELS

The same configuration used to validate the viscous–inviscid interaction model, is also used to demonstrate the applicability and usefulness of reduced-order models. The blades have chord c and are assumed to vibrate with reduced frequency $k = \omega c/v_\infty$ in a pitch motion about the mid-chord point. The upstream far-field Mach number M is 0·85. The interblade phase angle of the vibration of the airfoils is denoted by σ.

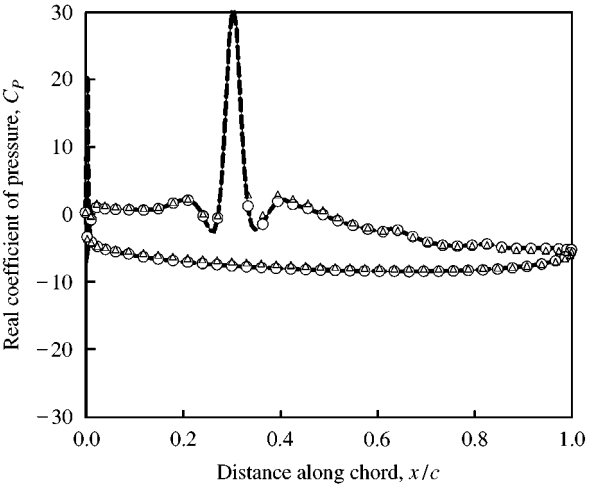

Figure 10. The real (in-phase) part of the unsteady coefficient of pressure C_P using the full model and various reduced-order models. All points essentially fall on a single curve, but some are omitted for the sake of clarity. —, Full model; - - -, 15-mode model (σ); ○, 15-mode model (k); △, 75-mode model (k and σ).

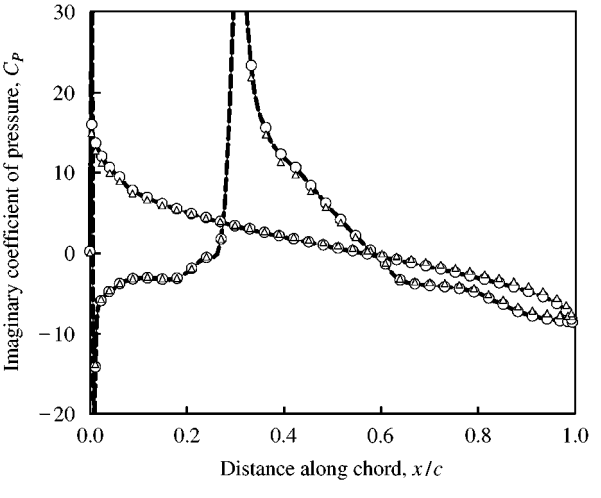

Figure 11. The imaginary (out-of-phase) part of the unsteady coefficient of pressure C_P using the full model and various reduced-order models. All points essentially fall on a single curve, but some are omitted for the sake of clarity. —, Full model; - - -, 15-mode model (σ); ○, 15-mode model (k); △, 75-mode model (k and σ).

Figures 10 and 11 show the real (in-phase) and imaginary (out-of-phase) coefficient of pressure obtained using the full model and three distinct reduced-order models. The reduced frequency k is 1·0, and the interblade phase angle σ is 90°. One reduced-order model was constructed using 15 modes obtained from 72 POD snapshots computed by varying the interblade phase angle uniformly from -180 to 180°. This reduced-order model is denoted by ROM-σ. Another reduced-order model was constructed using 15 modes obtained by computing 100 snapshots by varying the reduced frequency k uniformly between 0 and 2·75. This reduced-order model is denoted by ROM-k. The third reduced-order model used in Figures 10 and 11 was constructed using 75 modes obtained from 10×18 snapshots computed by varying both the interblade phase angle σ (10 values uniformly distributed between -180 and 180°) and the reduced frequency k (18 values uniformly distributed between 0 and 2·75). This reduced-order model is denoted by ROM-σ–k. The unsteady pressure distribution obtained with any of the three reduced-order models is shown to agree very well with the results provided by the full model. All points essentially fall on a single curve, but some are omitted for the sake of clarity.

Figure 12 shows the real (in-phase) part coefficient of lift obtained using the full model, the ROM-σ model (15-modes), and the ROM-σ–k (75 modes). The coefficient of lift obtained with the reduced-order models agree very well with the results obtained with the full model. A small number of modes (15) are required to model the entire range of interblade phase angles for a specific reduced frequency. However, a larger number of modes (75) is required when the reduced-order model is required to model the entire range of interblade phase angles and a large range of reduced frequencies. When compared with a subsonic reduced-order model (Epureanu *et al.* 2001), the transonic reduced-order model requires a larger number of POD modes. This may be due to the increased Mach number and the presence of the shock and the strong inviscid–viscous interaction in the shock area. A subsonic reduced-order model requires about 25 modes, whereas the transonic reduced-order model requires 75 modes. Nevertheless, the dimension (75) of the transonic reduced-order model is much smaller than the dimension of the original system. The reduction in dimension is about three orders of magnitude. Similar results are obtained for the imaginary (out-of-phase) part of the coefficient of lift, and are not shown here for the sake of brevity.

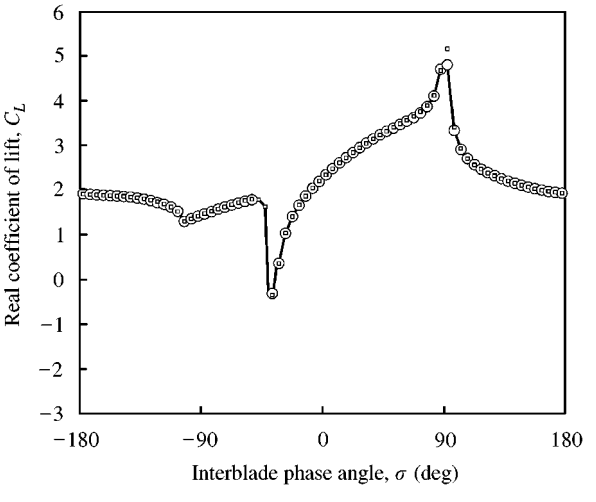

Figure 12. Real (in-phase) part of the unsteady coefficient of lift C_L using the full model and various reduced-order models. —, Full model; ○, 15-mode model (σ); □, 75-mode model (k and σ).

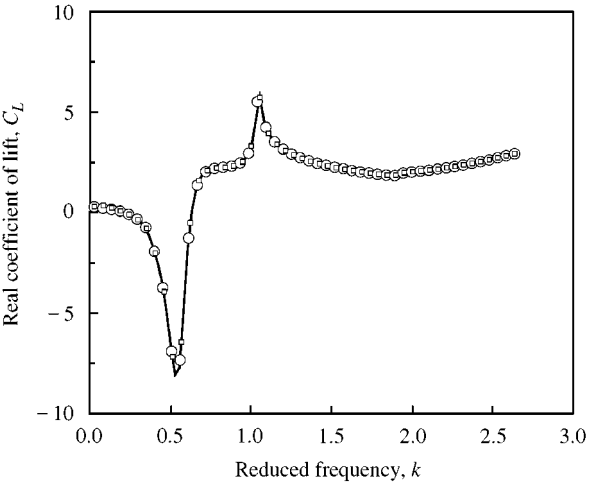

Figure 13. Real (in-phase) part of the unsteady coefficient of lift C_L using the full model and various reduced-order models. —, Full model; ○, 15-mode model (k); □, 75-mode model (k and σ).

Figure 13 shows the real (in-phase) part of the coefficient of lift for various reduced frequencies. The lift obtained using the full model is shown together with the lift obtained using two reduced-order models. One reduced-order model is the ROM-k model, which uses 15 modes. The other reduced-order model is ROM-σ–k model, which is the same model used in Figure 12 (75 modes). The lift computed using either reduced-order model are in very good agreement with the results obtained with the full model. A small number of modes is required to accurately model the system over a wide range of reduced frequencies when the interblade phase angle is maintained constant. Also, the more general reduced-order model is shown to accurately predict the dynamics of the system for a wide range of reduced frequencies. Similar results are obtained for the imaginary (out-of-phase) part of the coefficient of lift, not shown here for the sake of brevity.

The lower-dimensional models ROM-k and ROM-σ which use only 15 modes are specialized models. Their validity is limited to the range of parameters used for their construction. For example, the model ROM-k performs poorly if it is used to compute the flow for various interblade phase angles. The low performance is due to the fact that ROM-k is a specialized/tuned model, valid for an interblade phase angle of 90°. Similarly, the model ROM-σ performs poorly when used to compute the flow for various reduced frequencies. Although ROM-σ performs very well for a fixed reduced frequency k of 1, its performance is limited when used at other values of k. Nevertheless, the 75 mode model ROM-σ–k performs well for a full spectrum of interblade phase angles as well as a large range of reduced frequencies. The ROM-σ–k is not as specialized as ROM-k or ROM-σ, but is more general. The generality is provided by the increased number of POD modes used, from 15 in the case of ROM-k and ROM-σ to 75 in the case of ROM-σ–k.

7. CONCLUSIONS

Starting from a fully nonlinear unsteady model of the transonic flow in a turbomachinery cascade of blades, the nonlinear steady flow was first determined. Then the unsteady flow created by oscillating blades was calculated by linearizing the dynamic perturbation about the nonlinear steady flow. An inviscid–viscous flow model was used. The inviscid flow was described by the full-potential equation with appropriate upwinding in the transonic region.

The viscous flow near the airfoils and in the wakes was described by an integral boundary layer model.

A frequency domain solution was constructed for the unsteady perturbation of the flow field. The proper orthogonal decomposition technique was then applied to the frequency domain model to construct several reduced-order models of the transonic flow. Surely, if one only wants the aerodynamic information *per se*, then constructing the POD model takes about as much time as the original method. However, if one wants to combine the aerodynamic model with a structural model (not to mention an active control system), then the time saved is orders of magnitude because one is using a POD model with less than 100 degrees of freedom (as shown in this paper) versus using the original CFD model with more than 10 000 degrees of freedom. Thus, it is in the aeroelastic analysis that the time savings are primarily realized, not in generating the aerodynamic data *per se*. The purpose of constructing a POD model is then to put the basic physics of the original CFD model in a more compact form that is advantageous to those who do aeroelastic analyses.

A cascade of blades forming the Tenth Standard Configuration was investigated to show that the reduced-order model with only 15–75 degrees of freedom accurately predicts the unsteady response of the full system with approximately 15 000 degrees of freedom.

References

Ayer, T. C. & Verdon, J. M. 1998 Validation of a nonlinear unsteady aerodynamic simulator for vibrating blade rows. *Journal of Turbomachinery* **120,** 112–121.

Bienkiewicz, B. 1996 New tools in wind engineering. In *Proceedings of the 1994 East European Conference on Wind Engineering*, Warsaw, Poland, Vol. 65, pp. 297–300. Amsterdam: Elsevier.

Buffum, D. H., Capece, V. R., King, A. J. & El-Aini, Y. M. 1998 Oscillating cascade aerodynamics at large mean incidence. *Journal of Turbomachinery* **120,** 122–130.

Canuto, C., Hussaini, M. Y., Quarteroni, A. & Zang, T. A. 1988 *Spectral Methods in Fluid Dynamics*. New York: Springer-Verlag.

Catherall, D. & Mangler, K. W. 1966 The integration of the two dimensional laminar boundary layer equations past the point of vanishing skin friction. *Journal of Fluid Mechanics* **26,** 163–182.

Cebeci, T. & Bradshaw, P. 1977 *Momentum Transfer in Boundary Layers*. Washington, DC: Hemisphere Publishing Corporation.

Cedar, R. & Stow, P. 1985 The addition of quasi-three-dimensional terms into a finite element method for transonic turbomachinery blade-to-blade flows. *International Journal for Numerical Mehods in Fluids* **5,** 101–114.

Cenedese, A., Miozzi, M. & Querzoli, G. 1997 Comparison between fourier and proper orthogonal decomposition of a velocity field within a convective vessel. In *Proceedings of the Eighth International Conference on Computational Methods and Experimental Measurements*, Vol. 1, pp. 319–329, Rhodes, Greece. Computational Mechanics Publications.

Chambers, D. H., Adrian, R. J., Moin, P., Stewart, D. S. & Sung, H. J. 1988 Karhunen–Loève expansion of Burgers' model of turbulence. *Physics of Fluids* **31,** 2573–2582.

Cizmas, P. G. A. 1995 A simultaneously coupled potential—boundary layer model of stall flutter in turbomachinery. Ph.D. thesis, Duke University.

Cizmas, P. G. A. & Hall, K. C. 1995 Computation of steady and unsteady viscous flows using a simultaneously coupled inviscid–viscous ineraction technique. *Journal of Fluids and Structures* **9,** 639–657.

Clark, W. S. 1998 Investigation of unsteady viscous flows in turbomachinery using a linearized Navier–Stokes analysis. Ph.D. thesis, Duke University.

Deane, A. E., Kevrekidis, I. G., Karniadakis, G. E. & Orszag, S. A. 1988 Low-dimensional models for complex geometry flows: Application to grooved channels and circular cylinders. *Physics of Fluids* **3,** 2337–2354.

Dowell, E. H. 1980 A simple method for converting frequency domain aerodynamics to the time domain. NASA, Lewis Research Center.

Dowell, E. H. 1995 Eigenmode analysis in unsteady aerodynamics: Reduced-order models. In *Proceedings of the 36th AIAA/ASME/ASCE/AHS/ASC Structures, Structural Dynamics, and Materials Conference*, Vol. 1, pp. 1–13, New Orleans, LA. Washington, DC: AIAA.

Dowell, E. H., Hall, K. C., Thomas, J. P., Florea, R., Epureanu, B. I. & Heeg, J. 1999 Reduced-order models in unsteady aerodynamics. In *Proceedings of the 40th AIAA/ASME/ASCE/AHS/ASC Structures, Structural Dynamics, and Materials Conference*, St. Louis, Missouri, on CD-ROM, pp. 229–252. Washington, DC: AIAA.

Drela, M. 1986 Two-dimensional transonic aerodynamic design and analysis using the Euler equations. Ph.D. thesis, M.I.T.

Drela, M. 1996 Unsteady integral boundary layer equations with lag dissipation closure. Personal communication.

Epureanu, B. I. & Dowell, E. H. 1997 System identification for Ott–Grebogi–Yorke controller design. *Physical Review E* **56,** 5327–5331.

Epureanu, B. I. & Dowell, E. H. 1998 On the optimality of the OGY control scheme. *Physica D* **116,** 1–7.

Epureanu, B. I., Hall, K. C. & Dowell, E. H. 2001 Reduced-order models of unsteady viscous flows in turbomachinery using viscous–inviscid coupling. *Journal of Fluids and Structures* (to appear).

Epureanu, B. I., Trickey, S. T. & Dowell, E. H. 1998 Stabilization of unstable limit cycles in systems with limited controllability: expanding the basin of convergence of OGY-type controllers. *Nonlinear Dynamics*, **15,** 191–205.

Florea, R., Hall, K. C. & Cizmas, P. G. A. 1998 Reduced-order modeling of unsteady viscous flow in a compressor cascade. *AIAA Journal* **36,** 1039–1048.

Fransson, T. H. & Verdon, J. M. 1993 Panel discussion on standard configurations for unsteady flow through vibrating axial-flow turbomachine. In *Unsteady Aerodynamics, Aeroacoustics and Aeroelasticity of Turbomachines and Propellers* (ed. H. M. Atassi), Vol. 1, pp. 859–889. New York: Springer-Verlag.

Georgiou, I. T. & Schwartz, I. B. 1996 Proper orthogonal decomposition approach to coupled structural—mechanics systems. In *Nonlinear Dynamics and Controls*, DE-Vol. 91, pp. 7–12. New York: ASME.

Giles, M. B. 1985 Newton solution of steady two-dimensional transonic flow. Ph.D. thesis, Massachusetts Institute of Technology.

Green, J. E. 1976 Application of head's entrainment method to the prediction of turbulent boundary layers and wakes in compressible flows. Memoranda, Aeronautical Research Council.

Green, J. E., Weeks, D. J. & Brooman, J. W. F. 1976 Prediction of turbulent boundary layers and wakes in compressible flows by a lag entrainment method. Memoranda, Aeronautical Research Council.

Greitzer, E. M. 1976 Surge and rotating stall in axial flow compressors. Part I: theoretical compression system model. *ASME Journal of Engineering for Power* **98,** 190–198.

Habashi, W. G. & Hafez, M. M. 1982 Finite element solutions of transonic flow problems. *AIAA Journal* **20,** 1368–1376.

Habashi, W. G., Hafez, M. M. & Kotiuga, P. L. 1985 Computation of choked and supersonic trubomachinery flows by a modified potential method. *AIAA Journal* **23,** 214–220.

Hafez, M. M., South, J. & Murman, E. 1979 Artificial compressibility methods for numerical solutions of transonic full potential equation. *AIAA Journal* **17,** 838–844.

Hall, K. C. 1993 Deforming grid variational principle for unsteady small disturbances flows in cascades. *AIAA Journal* **31,** 891–900.

Hall, K. C. 1994 Eigenanalysis of unsteady flows about airfoils, cascades, and wings. *AIAA Journal* **32,** 2426–2432.

Hall, K. C., Florea, R. & Lanzkron, P. J. 1995 A reduced-order model of unsteay flows in turbomachinery. *Journal of Turbomachinery* **117,** 375–383.

Hall, K. C., Lorence, C. B. & Clark, W. S. 1993 Nonreflecting boundary conditions for linearized unsteady aerodynamic calculations. AIAA Paper 93-0882.

Hall, K. C., Thomas, J. P. & Dowell, E. H. 1999 Reduced-order modeling of unsteady small-disturbance flows using a frequency-domain proper orthogonal decomposition technique. In AIAA Paper 99-0655.

Ho, T. C. E., Davenport, A. G. & Surry, D. 1995 Characteristic pressure distribution shapes and load repetitions for the wind loading of low building roof panels. *Journal of Wind Engineering and Industrial Aerodynamics* **57,** 261–279.

Holmes, P., Lumley, J. L. & Berkooz, G. 1996 *Turbulence, Coherent Structures, Dynamical Systems and Symmetry*. Cambridge: Cambridge University Press.

Jeong, S. H. & Bienkiewicz, B. 1997 Application of autoregressive modeling in proper orthogonal decomposition of building wind pressure. In *Proceedings of the 3rd International Colloquium on*

Bluff Body Aerodynamics and Applications, Vol. 69–71, pp. 685–695, Blacksburg, VA. Amsterdam: Elsevier.

Kikuchi, H., Tamura, Y., Ueda, H. & Hibi, K. 1997 Dynamic wind pressures acting on a tall building model—proper orthogonal decomposition. In *Proceedings of the 3rd International Colloquium on Bluff Body Aerodynamics and Applications*, Vol. 69–71, pp. 631–646, Blacksburg, VA. Amsterdam: Elsevier.

Kim, T. 1998 Frequency domain Karhunen–Loéve method and its application to linear dynamic systems. *AIAA Journal* **36,** 2117–2123.

Kim, T., Nam, C. & Kim, Y. 1997 Reduced-order aeroservoelastic model with an unsteady aerodynamic eigenformulation. *AIAA Journal* **35,** 1087–1088.

Leballeur, J. C. 1978 Couplage visqueux-non-visqueux: méthode numerique et applications aux écoulements bidimensionnels transsoniques et supersoniques. *Recherche Aerospatiale* **2,** 65–76.

Liu, Z. C., Adrian, R. J. & Hanratty, P. 1994 Reynolds number similarity of orthogonal decomposition of the outer layer of turbulent wall flow. *Physics of Fluids* **6,** 2815–2819.

Mahajan, A. J., Dowell, E. H. & Bliss, D. B. 1991 Eigenvalue calculation procedure for Euler/Navier–Stokes solvers with application to flows over airfoils. *Journal of Computational Physics* **97,** 398–413.

Moore, F. K. & Greitzer, E. M. 1986 A theory of post-stall transients in axial compression systems: Parts I and II. *Journal of Engineering for Gas Turbines and Power* **108,** 68–76.

Murman, E. M. & Cole, J. D. 1971 Calculation of plane steady transonic flow. *AIAA Journal* **9,** 114–121.

Nishida, B. & Drela, M. 1995 Fully simultaneous coupling for three-dimensional viscous–inviscid flows. AIAA Paper 95-1806-CP.

Noor, A. K. 1994 Recent advances and applications of reduction methods. *Applied Mechanics Reviews*, **47,** 125–145.

Peterson, L. D. & Crawley, E. F. 1988 Improved exponential time series approximation of unsteady aerodynamic operators. *Journal of Aircraft* **25,** 121–127.

Romanowski, M. C. 1996 Reduced order unsteady aerodynamic and aeroelastic models using Karhunen–Loève eigenmodes. AIAA Paper 96-3981.

Sahan, R. A., Koc-sahan, N., Albin, D. C. & Liakopoulos, A. 1997 Artificial neural network - based modeling and intelligent control of transitional flows. In *Proceedings of the 1997 IEEE International Conference on Control Applications*, Vol. 1, pp. 359–364, Hartford, CT. New York: IEEE.

Sharma, O. P., Pickett, G. F. & Ni, R. H. 1992 Assesment of unsteady flows in turbines. *Journal of Turbomachinery* **114,** 79–90.

Shaw, S. W. & Pierre, C. 1993 Normal modes for non-linear vibratory systems. *Journal of Sound and Vibration* **164,** 85–124.

Shaw, S. W. & Pierre, C. 1994 Normal modes of vibration for non-linear continuous systems. *Journal of Sound and Vibration* **169,** 319–347.

Sirovich, L. 1987a Turbulence and the dynamics of coherent structures. Part I: coherent structures. *Quarterly of Applied Mathematics* **XLV,** 561–571.

Sirovich, L. 1987b Turbulence and the dynamics of coherent structures. Part II: symmetries and transformations. *Quarterly of Applied Mathematics* **XLV,** 573–582.

Sirovich, L. 1987c Turbulence and the dynamics of coherent structures. Part III: dynamics and scaling. *Quarterly of Applied Mathematics* **XLV,** 583–590.

Stone, E. & Cutler, A. 1996 Introduction to archetypal analysis of spatio-temporal dynamics. *Physica D* **96,** 110–131.

Strain, M. C. & Greenside, H. S. 1998 Size-dependent transition to high-dimensional chaotic dynamics in a two-dimensional excitable medium. *Physical Review Letters* **80,** 2306–2309.

Tamura, Y., Ueda, H., Kikuchi, H., Hibi, K., Suganuma, S. & Bienkiewicz, B. 1997 Proper orthogonal decomposition study of approach wind-building pressure correlation. *Journal of Wind Engineering and Industrial Aerodynamics* **72,** 421–431.

Tannehill, J. C., Anderson, D. A. & Pletcher, R. H. 1997 *Computational Fluid Mechanics and Heat Transfer*. London: Taylor & Francis.

Tatum, K. E. 1983 Finite element methods for transonic flow analysis. *AIAA Journal* **21,** 1071–1078.

Ueda, T. & Dowell, E. H. 1984 Flutter analysis using nonlinear aerodynamic forces. *Journal of Aircraft* **21,** 101–109.

Uematsu, Y., Yamada, M., Inoue, A. & Hongo, T. 1997 Wind loads and wind-induced dynamic behavior of a single-layer latticed dome. *Journal of Wind Engineering and Industrial Aerodynamics* **66,** 227–248.

VELDMAN, A. E. P. 1979 A numerical method for the calculation of laminar, incompressible boundary layers with strong viscous–inviscid interaction. National Aerospace Laboratory, NLR, The Netherlands.

VELDMAN, A. E. P. 1981 New quasi-simultaneous method to calculate interacting boundary layers. *AIAA Journal* **19,** 79–85.

WHITEHEAD, D. S. 1959 The vibration of cascade blades treated by actuator disk methods. *Proceedings of the Institution of Mechanical Engineers* **173,** 555–563.

WHITEHEAD, D. S. & NEWTON, S. G. 1985 A finite element method for the solution of two-dimensional transonic flows in cascades. *Journal of Computational Physics* **5,** 115–132.

WHITFIELD, D. L., SWAFFORD, T. W. & JACOCKS, J. L. 1981 Calculation of turbulent boundary layers with separation and viscous–inviscid interaction. *AIAA Journal* **19,** 1315–1322.